AGU PUBLICATIONS

Geophysical Research Letters

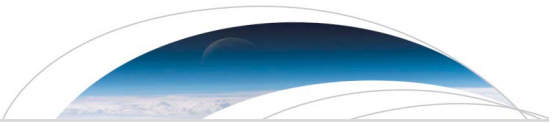

RESEARCH LETTER
10.1002/2017GL076042

Key Points:
- One hundred year geoelectric amplitudes show significant geographic granularity
- One hundred year geoelectric amplitudes resemble those for the March 1989 storm
- One hundred year geoelectric amplitudes are starkly different from NERC benchmarks

Supporting Information:
- Supporting Information S1

Correspondence to:
J. J. Love,
jlove@usgs.gov

Citation:
Love, J. J., Lucas, G. M., Kelbert, A., & Bedrosian, P. A. (2018). Geoelectric hazard maps for the Mid-Atlantic United States: 100 year extreme values and the 1989 magnetic storm. *Geophysical Research Letters*, *45*, 5–14. https://doi.org/10.1002/2017GL076042

Received 12 OCT 2017
Accepted 30 NOV 2017
Accepted article online 5 DEC 2017
Published online 4 JAN 2018

Geoelectric Hazard Maps for the Mid-Atlantic United States: 100 Year Extreme Values and the 1989 Magnetic Storm

Jeffrey J. Love[1], **Greg M. Lucas**[1], **Anna Kelbert**[1], **and Paul A. Bedrosian**[2]

[1]Geomagnetism Program, Geologic Hazards Science Center, U.S. Geological Survey, Denver, CO, USA, [2]Crustal Geophysics and Geochemistry Science Center, U.S. Geological Survey, Denver, CO, USA

Abstract Maps of extreme value geoelectric field amplitude are constructed for the Mid-Atlantic United States, a region with high population density and critically important power grid infrastructure. Geoelectric field time series for the years 1983–2014 are estimated by convolving Earth surface impedances obtained from 61 magnetotelluric survey sites across the Mid-Atlantic with historical 1 min (2 min Nyquist) measurements of geomagnetic variation obtained from a nearby observatory. Statistical models are fitted to the maximum geoelectric amplitudes occurring during magnetic storms, and extrapolations made to estimate threshold amplitudes only exceeded, on average, once per century. For the Mid-Atlantic region, 100 year geoelectric exceedance amplitudes have a range of almost 3 orders of magnitude (from 0.04 V/km at a site in southern Pennsylvania to 24.29 V/km at a site in central Virginia), and they have significant geographic granularity, all of which is due to site-to-site differences in magnetotelluric impedance. Maps of these 100 year exceedance amplitudes resemble those of the estimated geoelectric amplitudes attained during the March 1989 magnetic storm, and, in that sense, the March 1989 storm resembles what might be loosely called a "100 year" event. The geoelectric hazard maps reported here stand in stark contrast with the 100 year geoelectric benchmarks developed for the North American Electric Reliability Corporation.

1. Introduction

Geoelectric fields induced in the Earth's conducting interior during magnetic storms can interfere with the operation of electric-power grids (e.g., Boteler, 2001; Molinski, 2002; Samuelsson, 2013; Piccinelli & Krausmann, 2014). Notably, the magnetic storm of 13 March 1989 generated geoelectric fields that led to the collapse of the Hydro-Québec power grid system (Béland & Small, 2005; Bolduc, 2002). The same storm caused numerous operational problems in U.S. power grids and damaged a high-voltage transformer at a nuclear power plant (Barnes et al., 1991; North American Electric Reliability Corporation, 1990). Some scenario studies anticipate that the future occurrence of a rare but intense magnetic superstorm could cause a continental-scale loss of electric power transmission (e.g., Kappenman, 2012), for which the corresponding costs for national economies would be significant (Baker et al., 2008; Barnes & Van Dyke, 1990; Eastwood et al., 2017; Lloyd's of London, 2013). In response, the United States Federal Energy Regulatory Commission (2013, Order No. 779) directed the North American Electric Reliability Corporation (NERC) to assess the vulnerability of power grid systems to geomagnetic disturbance. This, in turn, motivated a study to estimate threshold geoelectric amplitudes that might only be exceeded (on average) across the continental United States once every 100 years (North American Electric Reliability Corporation, 2014).

In support of a National Science and Technology Council (2015, Goal 1.1) (NSTC) project for evaluating space weather hazards, we map extreme value (100 year) geoelectric amplitudes across the eastern, Mid-Atlantic region of the United States, stretching from southern Pennsylvania to northern North Carolina. This region encompasses the Philadelphia-Baltimore-Washington megalopolis; it has a high population density and critically important power grid systems that experienced operational problems during the 1989 magnetic storm. We construct our hazard maps by analyzing the statistics of long time series of geoelectric field amplitude obtained by convolving long time series of historical geomagnetic field variation, measured at a magnetic observatory, with empirical estimates of solid earth impedance, obtained during a magnetotelluric survey. Our regional analysis method is simpler and more direct than that recently used to map geoelectric hazards

across the continental United States (Love & Bedrosian, 2018; Love et al., 2016); a further distinction is that our method allows for analysis of geoelectric fields induced during specific magnetic storms (such as that of March 1989). As we will show, our estimates of geoelectric hazards across the Mid-Atlantic show both similarities and differences with those obtained by NERC.

2. Induction in a Conducting Earth

We briefly review some theoretical principles of geoelectromagnetism. At the Earth's surface, geomagnetic $\mathbf{B}(t,x,y)$ and geoelectric $\mathbf{E}(t,x,y)$ field variations are functions of time t and geographic location (x,y). As is often the case, it is convenient to work in a combination of the time domain and the Fourier-transformed (e.g., Bracewell, 2000) frequency domain,

$$\mathcal{F}\{\mathbf{B}(t)\} = \mathbf{B}(f) \text{ and } \mathcal{F}\{\mathbf{E}(t)\} = \mathbf{E}(f), \tag{1}$$

where f is the frequency of sinusoidal variation. We concentrate our attention on the horizontal Cartesian components (north $\hat{\mathbf{x}}$, east $\hat{\mathbf{y}}$) of the geomagnetic and the (induced) geoelectric fields,

$$\mathbf{B}_h(x,y) = [B_x, B_y] \text{ and } \mathbf{E}_h(x,y) = [E_x, E_y]. \tag{2}$$

In the Earth's interior, geomagnetic and geoelectric variation in the frequency range of interest here (section 3) can be described in terms of the classical laws of "quasi-static" electromagnetism (no displacement current) for an electrically conducting medium (e.g., Stratton, 1941, chapter 5). In this case, the relationship between the geomagnetic and geoelectric fields at the Earth's surface can be summarized in terms of a linear transfer equation,

$$\mathbf{E}_h(f,x,y) = \frac{1}{\mu}\mathbf{Z}(f,x,y) \cdot \mathbf{B}_h(f,x,y) \tag{3}$$

(e.g., Berdichevsky & Dmitriev, 2008; Weidelt & Chave, 2012), where μ is permeability. The impedance tensor $\mathbf{Z}$ is frequency dependent and complex (it has real and imaginary parts); for a given geomagnetic vector $\mathbf{B}_h$, the impedance $\mathbf{Z}$ specifies the amplitude, polarization, and phase of the geoelectric field $\mathbf{E}_h$. Impedance has units of ohms (Ω); the transfer tensor $\mathbf{Z}/\mu$ has units of (V/km)/nT. With inverse Fourier transformation, equation (3) can be recognized as a convolution in the time domain (e.g., Bracewell, 2000, chapter 3),

$$\mathbf{E}_h(t,x,y) = \frac{1}{\mu}\left(\mathbf{Z} * \mathbf{B}_h\right)(t,x,y). \tag{4}$$

Equations (3) and (4) are the basis for our calculations and results. The impedance tensor $\mathbf{Z}$, itself, is a nonlinear function of the Earth's internal conductivity structure $\sigma(\mathbf{r})$, where $\mathbf{r}$ is the position vector (e.g., Hermance, 2011). Rock conductivity, in turn, depends on a myriad of properties, including mineral content, melt, and solid phase, water content, clay content, porosity, and cracks and grain boundaries (e.g., Evans, 2012; Yoshino, 2011); the spatial distribution of these properties (and, by proxy, conductivity) within the Earth is reflective of geological history and structure (e.g., Palacky, 1988). In qualitative terms, field variation having frequency f is attenuated as a skin effect within a volume of rock beneath the site. Apparent conductivity and diffusive skin depth are given by

$$\sigma_A(f) \simeq \frac{2\pi\mu f}{|\mathbf{Z}(f)|^2} \text{ and } \delta_A(f) \simeq \sqrt{\frac{1}{\pi\mu f \sigma_A(f)}}, \tag{5}$$

for some tensor norm $|\cdot|$; we choose the Frobenius norm (e.g., Berdichevsky & Dmitriev, 2008, chapter 2.6). Since electromagnetic induction is sensitive to structure within a fraction of a skin depth, as evident from examination of linearized data sensitivity over a half space (e.g., Schwalenberg et al., 2002), we chose a shorter length scale, $\delta_A/10$, as a proxy indicator for where induction is focused within the Earth at a given variational period.

3. Magnetotelluric Tensors

Informed by the preceding physical summary, we recognize that geoelectric time series $\mathbf{E}_h(t)$ can be reconstructed using measurements of Earth impedance and historical records of geomagnetic field variation

(e.g., Pirjola, 2002). For **Z**, we use magnetotelluric impedance tensors (Schultz et al., 2006) acquired during a survey of the continental United States (Schultz, 2010) as part of the National Science Foundation's EarthScope project (Williams et al., 2010). Each of these tensors was constructed (Egbert, 2007) from measurements of geomagnetic and geoelectric field variation made simultaneously at a given survey site using temporarily deployed electromagnetic sensors (e.g., Ferguson, 2012). For this analysis, we choose 61 tensors constructed from survey data collected between 2015 and 2017 within a $\sim 600 \times 600$ km^2 region defined by the latitude-longitude square (35.20° – 41.20°N, 74.40° – 80.40°W) and covering the Mid-Atlantic United States; the tensors correspond to survey sites having a 70 km nominal spacing; they are well defined within a frequency band of 10^{-4} to 10^{-1} Hz (periods of 10,000 to 10 s), and their errors are estimated to be less than 5% (Schultz, 2010). The EarthScope database (Kelbert et al., 2011) includes a quality rating for each tensor; we choose those with quality rating of 3 or higher, and in cases where multiple nearby sitings have been performed, to avoid redundancy, we use the tensor with the highest quality rating.

4. Magnetic Observatory Time Series

Storm-time geomagnetic disturbance is generated by electric currents (in the ionosphere and magnetosphere) at heights greater than about 100 km. By purely geometric attenuation, the horizontal length scale characterizing ground level geomagnetic variation will generally exceed 100 km. More specifically, analysis of 1 min, horizontal component geomagnetic variation (at high latitudes that are more active than the midlatitude Mid-Atlantic) shows reasonably good coherence in signals recorded by magnetometers separated in latitude by ~200 km (Watermann et al., 2006). Therefore, we assume that the 1 min, horizontal component variation measured at the U.S. Geological Survey (USGS) Fredericksburg (FRD), Virginia magnetic observatory (Love & Finn, 2011), located in the middle of the chosen $\sim 600 \times 600$ km latitude-longitude square region, is representative of geomagnetic variation across this region.

Geomagnetic vector data are recorded at the FRD observatory as discrete, time-sequential samples, denoted t_i for $i = 1, 2, 3, \ldots$, with a constant 1 min $= t_i - t_{i-1}$ sampling interval. Sinusoidal signals with periods shorter than 2 min are suppressed by analog and digital filters. We use "definitive" data covering the years 1983 – 2014; these have been calibrated for sensor drift and cleaned of artificial spikes and offsets. The 32 year long FRD time series is 97.7% complete; there are 16,454,755 1 min geomagnetic vector samples with very few gaps, mostly realized in the early 1980s. The longest gap in the FRD time series is 18 days 20 min in duration, beginning on 5 September 1983 at 17:00 UT; during this gap period, a small magnetic storm on 15 September was not recorded, maximum $-Dst = 58$ nT. In Figure 1a we plot FRD $\mathbf{B}_h(t_i)$ time series recording the March 1989 magnetic storm, which commenced at 01:28 UT on 13 March. In terms of standard geomagnetic indices (e.g., Menvielle et al., 2011), the global storm-time disturbance index reached a maximum $-Dst = 589$ nT at 01:30 UT on 14 March (the highest value since *Dst* was initiated in 1957) (e.g., Allen et al., 1989), the local *K* activity index reached the maximum defined value of 9 from 09:00 – 12:00 UT, 13 March and from 18:00 UT, 13 March to 03:00 UT, 14 March.

5. Numerical Convolution

We use computer-based algorithms to implement the time domain convolution represented by equations (3) and (4). First, we detrend the 1 min FRD time series $\mathbf{B}_h(t_i)$ by subtracting a second-order polynomial fitted to the entire 1983 – 2014 duration of the time series, and we fill (the few) data gaps in the time series by linear interpolation. Next, we apply a fast Fourier transform (e.g., Bracewell, 2000, chapter 11) with 64 bit precision to the entire FRD $\mathbf{B}_h(t_i)$, obtaining its (discrete) frequency domain expression, $\mathbf{B}_h(f_i)$. We then multiply this by a discrete sampling of the transfer tensor $\mathbf{Z}\left(f_i, x, y\right)/\mu$ for each survey site (x, y). And, finally, we apply an inverse fast Fourier transform to obtain discrete 1 min geoelectric time series $\mathbf{E}_h(t_i, x, y)$ for each site. Our algorithms have been tested against the geoelectric time series collected at a magnetic observatory (Fujii et al., 2015, KAK); errors in estimated $\mathbf{E}_h(t_i, x, y)$ are typically about 20% of the amplitude of $\mathbf{E}_h(t, x, y)$.

6. Geoelectric Time Series

In Figure 1b we plot $\mathbf{E}_h(t_i, x, y)$ time series for the March 1989 storm for the EarthScope survey site denoted VAQ58, located near Richmond, Virginia. From this plot, we see that geoelectric disturbance levels are generally high when geomagnetic disturbance levels are high. Maximum geoelectric field amplitude was attained at 21:45 UT on 13 March 1989, with $E_x = -9.86$ V/km and $E_y = 17.37$ V/km. This peak amplitude was almost

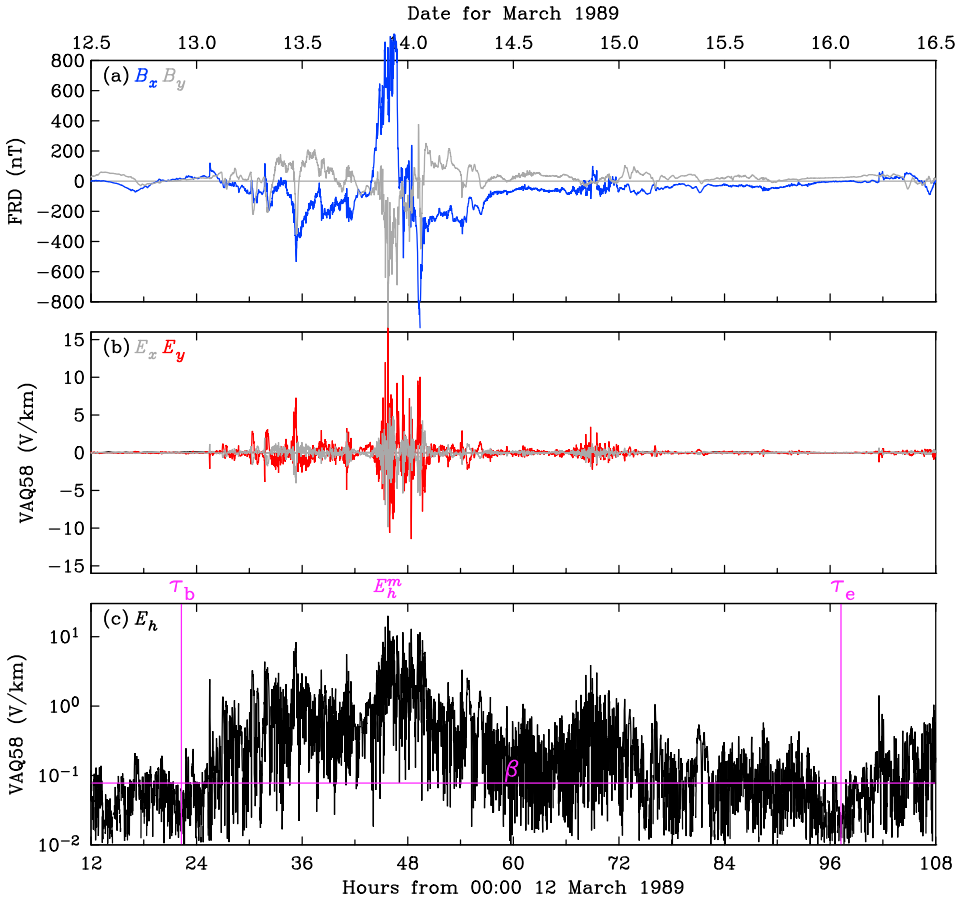

Figure 1. Time series of 1 min resolution (a) north $B_x(t_i)$ and east $B_y(t_i)$ component variation recorded at the USGS Fredericksburg, Virginia (FRD), observatory (geographic: 38.20°N, 77.37°W; geomagnetic for year 2000: 48.41°N, 6.89°W) during the magnetic storm of March 1989; and (b) corresponding geoelectric north $E_x(t_i)$ and east $E_y(t)$ component variation calculated for the EarthScope magnetotelluric survey site VAQ58 (37.38°N, 77.58°W) and (c) on a semilog plot, $E_h(t_i)$ together with parameters (purple) illustrating the algorithm used to select the local maximum E_h^m and exclude values within the disturbance period from τ_b to τ_e defined relative to the threshold β.

simultaneous with the tripping of compensators that led to the blackout of the Hydro-Québec power grid system in Canada (Bolduc, 2002). Over the subsequent several hours of the magnetic storm, numerous operational anomalies were reported by electric power companies in the Mid-Atlantic United States, including for the Allegheny Power System, the Pennsylvania-New Jersey-Maryland Interconnection, and Virginia Power (North American Electric Reliability Corporation, 1990).

7. Statistical Analysis and 100 Year Extremes

In constructing geoelectric hazard maps, we are inspired by research on earthquakes and landslides, where a "hazard" is defined as the probability that a potentially damaging event will have a size exceeding a certain threshold, occurring within a specified window of time, and located within a given geographic area (e.g., Varnes, 1984, p. 10; Panel on Seismic Hazard Analysis, 1988, p. 94; Smolka, 2006). In that light, we analyze the extreme value statistics of the largest 1˜min geoelectric amplitudes

$$E_h(t_i, x, y) = \sqrt{E_x^2 + E_y^2}, \tag{6}$$

at the various magnetotelluric survey sites (x, y) in our study area of the Mid-Atlantic. For each site and for the years 1983–2014, we need to identify maximum geoelectric amplitudes for each period of magnetic storm disturbance. Recognizing that extremely high geoelectric amplitudes are rare, while low amplitudes are common, we use a simple, numerically intensive algorithm, similar to that used by Love et al. (2015), that ranks

and winnows the 1 min E_h values. First, all of the E_h values are ranked by size; the maximum value E_h^m is identified; it is set aside for statistical analysis, and a 1 order-of-magnitude range is defined by the largest E_h^m value and a minimum E_{min}. Next, referring to Figure 1c, a threshold β is chosen for each survey site that is less than E_{min} but greater than the geometric average of all the E_h; with this, an interval of storm disturbance is defined by the last (first) moment τ_b (τ_e) in time before (after) E_h^m such that all E_h values within a sliding 1 h window are less than β; the E_h values within this interval are excluded from further analysis. The remaining E_h values are ranked, the next local maximum E_h^m value is identified and kept, and other surrounding disturbance values are excluded, etc.; this process is terminated when the highest remaining E_h value falls below E_{min}; then, as a quality check, the intervals identified as storm disturbance are visually inspected, especially those with maxima just above E_h^m. This ranking-and-winnowing algorithm removes most of the autocorrelation in the E_h time series, and it leaves us with several tens of E_h^m values for each survey site. For the years 1983–2014 and for most Mid-Atlantic sites, the highest E_h^m occurred during the March 1989 magnetic storm, but for a few sites, the highest E_h^m occurs during the magnetic storm of July 2000.

The largest E_h^m values lie in the tail of an extreme value distribution, with which we seek a reasonable extrapolation to an E_h^m amplitude that is only, on average, exceeded once per 100 years. To identify a distribution, we need a model of a statistical process. Following on from related work (e.g., Love et al., 2015; Pulkkinen et al., 2008), we consider a lognormal process (e.g., Aitchison & Brown, 1957; Crow & Shimizu, 1988), for which the probability density function is

$$f_{\mathcal{L}}(E_h^m|E_{\text{min}},\upsilon,\epsilon^2) = \frac{1}{E_h^m\sqrt{2\pi\epsilon^2}}\exp\left[-\frac{(\ln E_h^m-\upsilon)^2}{2\epsilon^2}\right], \tag{7}$$

where υ and ϵ^2 are parameters. A lognormal process can be realized from the multiplication of numerous underlying random variables, each of which is positive and drawn from well-behaved and independent distributions. Considering that, then, we recognize that the amplitude of the geoelectric field at a given geographic site is determined by the multiplication of several different physical factors. We have noted that geoelectric fields can be calculated by time domain convolution of Earth impedance with geomagnetic field variation, equations (3) and (4). And while surface impedance can be a complicated function of geographic location (x, y) and frequency f, impedance is time invariant and independent of geomagnetic variation. On the other hand, storm-time geomagnetic disturbance is driven by the multiplicative action of several solar wind parameters, such as plasma density and velocity (e.g., Kamide & Baumjohann, 1993), and while these might be lognormally distributed (e.g., Veselovsky et al., 2010), they are not completely independent. It is important to remain mindful of these qualifications, even if an amalgamation of geophysical and heliophysical variables is sufficient to give rise to extreme value E_h^m having a lognormal distribution.

Extreme value analyses often include comparisons with power law models (e.g., Newman, 2005; Turcotte, 1997), for which the probability density function is

$$f_{\mathcal{P}}(E_h^m|E_{\text{min}},\alpha) = \frac{\alpha-1}{E_{\text{min}}}\left(\frac{E_h^m}{E_{\text{min}}}\right)^{-\alpha}, \tag{8}$$

for positive parameter α and positive data $E_h^m > E_{\text{min}}$. A power law process can arise with minor modification of a lognormal process, for example, by imposing a nonzero lower bound on the allowed value of the data or by adding an underlying variable that acts additively (instead of multiplicatively) (e.g., Mitzenmacher, 2004; Newman, 2005, section G). While such hypothetical modifications might be realized, without physical justification for their existence, we prefer to use the "unmodified" lognormal distribution as a model of extreme value E_h^m.

Using a maximum likelihood algorithm (e.g., James, 2006, chapter 8.3), we estimate the lognormal $\{\upsilon,\epsilon^2\}$ and the power law $\{\alpha\}$ parameters for the E_h^m values for each survey site. In Figure 2, we show the cumulative number of occurrences per year that exceed E_h^m for the years 1983–2014 for VAQ55, VAQ58, and VAQ60, located, respectively, in western, central, and eastern Virginia. It is noteworthy that the amplitude of geoelectric disturbance differs greatly from one site to another—the difference between VAQ58 and VAQ55 is approximately a factor of 500—this is entirely due to localized differences in impedance (e.g., Bedrosian & Love, 2015; McKay & Whaler, 2006) caused by differences in complicated subsurface conductivity structure.

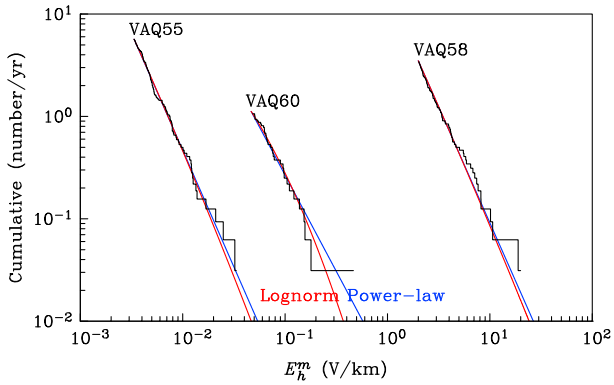

Figure 2. Cumulative number of times per year that storm maximum amplitude exceeds the threshold E_h^m (black) calculated for EarthScope Virginia sites VAQ58 (37.38°N, 77.58°W; 112 values), VAQ60 (37.13°N, 75.96°W; 36 values), VAQ55 (37.88°N, 79.81°W; 184 values) for years 1983–2014, together with fitted (red) lognormal and (blue) power law statistical models. The intersection of the model with the horizontal axis amounts to an extrapolated 100 year threshold value.

In the same figure, we show the cumulatives of the fitted lognormal and power law models given by

$$A \cdot \int_{E_h^m}^{\infty} f_{\mathcal{L},\mathcal{P}}(\xi)\mathrm{d}\xi, \tag{9}$$

where A is a normalizing factor. Both lognormal and power law models appear to provide reasonably good representations of the data. For VAQ55 and VAQ58, the lognormal fits closely resemble the power law fits, something often realized when fitting a finite range of data (e.g., Newman, 2005, section G). On the other hand, for VAQ60, the lognormal fit, with its curvature, is noticeably different from the power law. The Kolmogorov-Smirnov p-value (e.g., James, 2006, chapter 11.4.2) gives the probability that E_h^m values, similar to those estimated, could be realized from a hypothetical model; for VAQ58, for the lognormal distribution, the p-value is 0.60, and for the power law it is 0.66—in other words, neither model can be easily rejected; for VAQ55, the p-value are, respectively, 0.36 and 0.37; for VAQ60, they are 0.88 and 0.51. From the fitted models, we can estimate, as extrapolations, geoelectric amplitudes that are exceeded, on average, once every 100 years; in Figure 2, these correspond to the intersections of the models with the horizontal axis. For VAQ55 and VAQ58, the 100 year extrapolations of the lognormal model are similar to those for the power law model; the situation is very different, however, for VAQ60, where the 100 year lognormal extrapolation is 0.37 V/km, and the 100 year power law extrapolation is 0.58 V/km. This example illustrates the $E_h^m \to \infty$ asymptotic properties of the lognormal and power law models—an extreme value extrapolation of a fitted lognormal model will generally be less than that for a fitted power law model, and, in that sense, our preference for the lognormal model is "conservative."

We use the bootstrap method (e.g., Efron & Tibshirani, 1993) to estimate our confidence in the 100 year lognormal extrapolations. The ("mother") E_h^m values for each site are treated as a population distribution from which samples are drawn randomly with replacement. For each of numerous empirical data sets having size equal to that of the mother data set, we fit lognormal function using the maximum likelihood algorithm. From these fits, we estimate a median m for the 100 year extrapolation and corresponding lower l and upper u values for a centered 67% confidence interval; and among the various sites, [$l \simeq 0.75 \times m$, m, $u \simeq 1.34 \times m$], where $m \simeq 100$ year mother value; for VAQ58, specifically, [20.49, 25.12, 31.08] V/km.

8. One Hundred Year and 1989 Hazard Maps

In Figure 3a, we plot a color-coded map of extrapolated 100 year geoelectric exceedance amplitudes E_h^m for the Mid-Atlantic United States. Among the surveyed sites, the 100 year E_h^m amplitude is highest at VAQ58 at 24.29 V/km, and it is lowest at VAQ55 at 0.05 V/km; 100 year amplitudes exceed 10 V/km at 4 of the 61 sites and exceed 3 V/km at 15 of the 61 sites. Results such as these need to be properly interpreted—the map in Figure 3a depicts point wise statistical estimates of thresholds in geoelectric amplitude that are only exceeded, on average, once per century; the map does not show geoelectric amplitudes occurring during a single intense storm. Indeed, when a 100 year geoelectric amplitude is exceeded for a particular storm and at a particular site, it might not be attained for another site during the same storm. It is worth emphasizing that the extrapolated results shown in Figure 3a are relatively insensitive to inclusion of the March 1989 extreme value; for example, without the 1989 extreme value, for VAQ58, the 100 year exceedance E_h^m is 23.80 V/km, or just 0.49 V/km lower than if the 1989 extreme value were included.

For comparison, in Figure 3b, we plot the maximum E_h^m amplitudes that occurred during the March 1989 magnetic storm (this is not a statistical extrapolation). It is noteworthy that only small differences are seen between Figures 3a and 3b; the maximum E_h^m that occurred at VAQ58 during 1989 was 19.98 V/km. Furthermore, during the 1989 storm, E_h^m exceeded 10 V/km at 4 of the 61 sites considered; it exceeded 3 V/km at 12 of the 61 sites. The similarity between 100 year and the 1989 amplitudes is further illustrated in Figure 4, where we plot the cumulative for the amplitudes from all the Mid-Atlantic survey sites. Here, we see that the geoelectric amplitudes attained during the 1989 storm were only slightly less than our estimated 100 year exceedances.

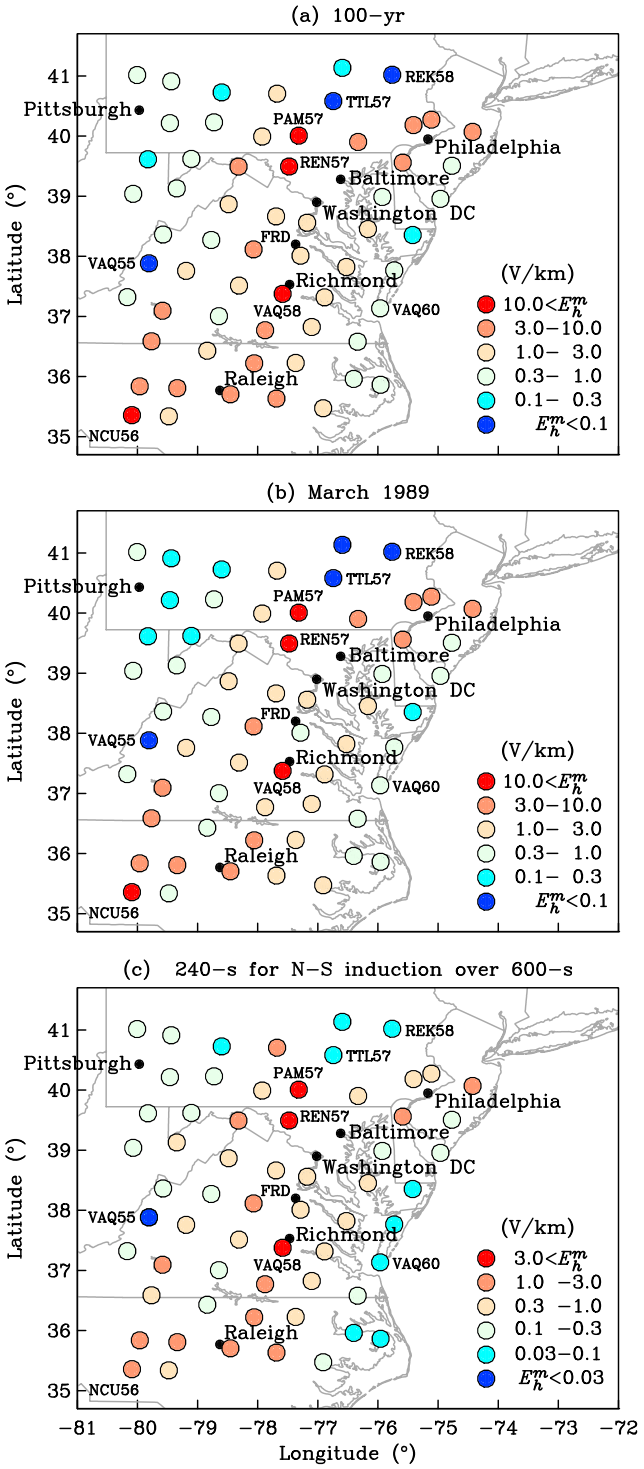

Figure 3. Maps showing (a) 100 year geoelectric exceedance amplitudes at the various EarthScope magnetotelluric survey sites across the Mid-Atlantic region of the United States, (b) maximum E_h^m that occurred during March 1989 magnetic storm, (c) 100 year geoelectric exceedance amplitudes for $B_x(t)$ geomagnetic waveforms having a 4 min period and persisting over a 10 min window of time (Love & Bedrosian, 2018). Note that the amplitude-color scale in Figure 3c is lower than in those in Figures 3a and 3b. The amplitudes shown in Figures 3a and 3b are given as Table S1 in supporting information.

In this respect, the induction intensity of the 1989 storm was nearly a "100 year event" for many places across the Mid-Atlantic.

In Figure 3c, we compare our hazard estimates with those obtained previously for the continental United States (Love & Bedrosian, 2018; Love et al., 2016) as part of a National Science and Technology Council (2015, Goal 1.1) (NSTC) project. Whereas the 1 min E_h^m analyzed here are samples from time series calculated by simply convolving a geomagnetic time series with magnetotelluric impedances, the hazard maps for the continental United States are indirectly derived: a statistical analysis is performed of historical global geomagnetic variation in terms of the amplitudes of waveforms having specific periods and measured over short windows of time; the waveforms are convolved with magnetotelluric impedances from various sites. These technical distinctions are responsible for our maps of E_h^m amplitudes being higher than those estimated by Love and Bedrosian (2018); they found, for example, 6.92 V/km at VAQ58 for north-south 4 min geomagnetic variation persisting over 10 min; the cumulative values from Love and Bedrosian (2018) are shown in Figure 4. Otherwise, the geographic form of the hazard maps is almost identical; amplitudes are relatively high at PAM57, Pennsylvania, REN57, Maryland, and NCU56, North Carolina; and they are relatively low at TTL57 and REK58, eastern Pennsylvania, and at VAQ55, western Virginia.

Our results should be compared with the 100 year benchmarks developed for the North American Electric Reliability Corporation (2014) that are based on a latitude-dependent statistical model of ground level geomagnetic disturbance (Pulkkinen et al., 2012) and impedances derived from one-dimensional (1-D), depth-dependent models of Earth conductivity for broad physiographic regions of North America (Blum et al., 2015; Ferguson & Odwar, 1997; Fernberg, 2012). Two of these physiographic regions, CP1 and PT1, cover most of the geographic area of our analysis; for the FRD latitude, the NERC 100 year geoelectric benchmarks are, respectively, 1.62 V/km and 2.34 V/km. From Figure 4, we see that the NERC benchmarks are higher than the median of both our estimated 100 year E_h^m exceedances and those for March 1989. But the intensity of the average of the geoelectric vector field across the 61 Mid-Atlantic survey sites attained 2.08 V/km at 21:45 on 13 March 1989—above the two NERC benchmark values for CP1 and PT1—and the NERC benchmarks do not come close to capturing the nearly 3 order of magnitude range we estimate for both 100 year exceedances and the 1989 storm. We note, furthermore, that our highest estimated E_h^m for 1989 are much higher than those found by Wei et al. (2013), who used the same 1-D Earth conductivity models used by NERC. Shortcomings in the 1-D conductivity models used by NERC have already been identified—they are only qualitatively derived from a literature survey, and they rely on few direct measurements (e.g., Bedrosian & Love, 2015; Love et al., 2016).

9. Discussion

The Mid-Atlantic region of the United States has, over more than a billion years, been shaped by plate tectonic continental collisions and riftings (e.g., Whitmeyer et al., 2007). The Grenville, Taconic, Acadian, and Alleghenian orogenies (e.g., Hatcher, 2005; Rast, 1989) created southwest to northeast trending mountain belts and basement uplifts (e.g., King et al., 1974). Deep beneath the Mid-Atlantic landscape are ancient rock formations that have been metamorphosed and welded together by heat and pressure. Geophysicists have only just begun to map the electrical conductivity structure of this complicated part of the Earth (e.g., Ogawa et al., 1996; Murphy & Egbert, 2017).

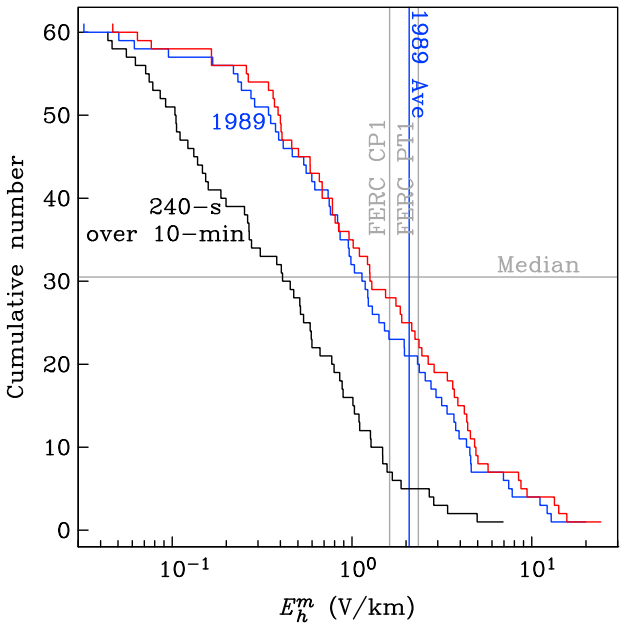

Figure 4. Cumulative of the 100 year geoelectric exceedance amplitudes (red), maximum geoelectric amplitudes attained for the March 1989 magnetic storm (blue), and values from Love and Bedrosian (2018) for north-south 4 min geomagnetic variation persisting over 10 min (black), each from all 61 considered survey sites in the Mid-Atlantic United States. Also shown are the NERC geoelectric benchmark values for the Coastal Plain CP1 and Piedmont PT1 physiographic regions, and the maximum intensity of the regional average of the geoelectric vector field attained on 13 March 1989.

Here we note that the effect of crustal conductivity structure, itself related to Mid-Atlantic geological structure, is evident in our maps of geoelectric hazards. Generally, low geoelectric hazards are seen in the northwest portion of Figure 3, surrounding Pittsburgh, Pennsylvania, a part of the Appalachian Plateau with electrically conductive sedimentary basins. Similarly, low geoelectric hazards are seen along the Mid-Atlantic Coastal Plain, a region covered by sediments that eroded from the mountains to the west. In more detail, survey site VAQ55, western Virginia, is located on the sedimentary rocks of the fold and thrust fault belt that is the Appalachian Valley and Ridge; for geomagnetic variation with a period of 2 min (Nyquist for the $\mathbf{B}(t_i)$ data analyzed, here), and using equation (5), we estimate the apparent conductivity for this site as $\sigma_A \simeq 0.99$ S/m and infer that induction is focused at very shallow depths, $\delta_A/10 \simeq 550$ m. High geoelectric hazards are seen in the electrically resistive "crystalline Appalachians" that run southwest to northeast, from around Raleigh, North Carolina, up to west of Philadelphia, Pennsylvania, in Figure 3; the Blue Ridge Mountains consist of the metamorphosed basement rocks, and the Piedmont consists of igneous rocks and a metamorphosed assembly of island arc and microcontinental terranes. Survey site VAQ58, with distinctly higher geoelectric hazards than neighboring sites, is located on a formation known as the Petersburg batholith, a large igneous intrusion within the Piedmont (e.g., Gates & Glover III, 1989); for geomagnetic variation with a period of 2 min, we estimate the apparent conductivity for this site as $\sigma_A \simeq 1.26 \times 10^{-5}$ S/m with induction occurring throughout the crustal column $\delta_A/10 \simeq 150$ km.

A curiosity of our results is the seeming lack of a clear "coast effect"—a localized distortion (and possible relative enhancement) of the geoelectric field caused by the conductivity contrast between continental crust and seawater (e.g., Lilley, 2007; Pirjola, 2013). The coast effect is another effect of 3-D conductivity structure, but where geographic differences in surface impedance are related to the presence of the ocean. We speculate that a coast effect might be obscured in our maps of geoelectric hazard by the complex shape of the Mid-Atlantic coast and the relatively shallow depth of the near-coast ocean. The Chesapeake Bay, which forms the eastern coast of Virginia and the inland bay of Maryland, is only about 6 m deep on average, but the diffusive skin depth for a half-space of seawater at 2 min is $\delta_A \simeq 3$ km—in other words, the near-coast ocean is possibly too shallow to have an appreciable effect on the geoelectric fields analyzed here. Other factors might further obscure a coast effect, including relatively conductive coastal-plane sediments that continue offshore and over the continental shelf (under the ocean) for over 100 km, the spatial complexity of the Mid-Atlantic's solid earth conductivity structure, and it is also possible that the geographic spacing of the EarthScope survey sites is too sparse to resolve a coast effect. Although additional investigation of a possible Mid-Atlantic coast effect might be worthwhile, the empirical results presented here remain valid regardless of any physical explanations.

Acknowledgments
We thank C. A. Finn, J. McCarthy, E. J. Riger, J. L. Slate, and two anonymous persons for reviewing a draft manuscript. This work was supported by the USGS Geomagnetism Program; G. M. Lucas is supported by a USGS Mendenhall post-doctoral fellowship. Magnetic observatory data used in this analysis are available from the USGS Geomagnetism Program (www.usgs.gov; 1983–2014); some of them can be obtained from INTERMAGNET (www.intermagnet.org; 1991–2014). EarthScope impedance tensors can be obtained from the Data Management Center of the Incorporated Research Institutions for Seismology (ds.iris.edu/ds/products/emtf) (Kelbert et al., 2011).

References

Aitchison, J., & Brown, J. A. C. (1957). *The lognormal distribution: With special reference to its uses in economics* (pp. 1–17). Cambridge, UK: Cambridge University Press.

Allen, J., Frank, L., Sauer, H., & Reiff, P. (1989). Effects of the March 1989 solar activity. *Eos, Transactions American Geophysical Union*, *70*(46), 1479–1488. https://doi.org/10.1029/89EO00409

Baker, D. N., et al. (2008). *Severe space weather events—Understanding societal and economic impacts* (pp. 1–144). Washington, DC: The National Academy Press. https://doi.org/10.17226/12507

Barnes, P. R., & Van Dyke, J. W. (1990). Economic consequences of geomagnetic storms (a summary). *IEEE Power Engineering Review*, *10*(11), 3–4. https://doi.org/10.1109/39.60450

Barnes, P. R., Rizy, D. T., McConnell, B. W., Tesche, F. M., & Taylor Jr., E. R. (1991). *Electric utility industry experience with geomagnetic disturbances* (Vol. ORNL-6665, pp. 1–78). Oak Ridge, TN: Oak Ridge National Laboratory.

Bedrosian, P. A., & Love, J. J. (2015). Mapping geoelectric fields during magnetic storms: Synthetic analysis of empirical United States impedances. *Geophysical Research Letters*, *42*, 10,160–10,170. https://doi.org/10.1002/2015GL066636

Béland, J., & Small, K. (2005). Space weather effects on power transmission systems: The cases of Hydro-Quebéc and Transpower New Zealand Ltd. In I. A. Daglis (Ed.), *Effects of Space Weather on Technology Infrastructure* (pp. 287–299). Dordrecht, Netherlands: Springer.

Berdichevsky, M. N., & Dmitriev, V. I. (2008). *Models and methods of magnetotellurics* (pp. 1–563). Berlin, Germany: Springer-Verlag.

Blum, C., Love, J. J., Pedrie, K., Bedrosian, P. A., & Rigler, E. J. (2015). A one-dimensional model of solid-earth electrical resistivity beneath Florida. *USGS Open-File Reports*, *98-782*, 1–16. https://doi.org/10.3133/ofr20151185

Bolduc, L. (2002). GIC observations and studies in the Hydro-Québec power system. *Journal of Atmospheric and Solar-Terrestrial Physics*, *64*(16), 1793–1802. https://doi.org/10.1016/S1364-6826(02)00128-1

Boteler, D. H. (2001). Space weather effects on power systems. In P. Song, H. J. Singer, & G. L. Siscoe (Eds.), *Space Weather, Geophysical Monograph Series* (Vol. 125, pp. 347–352). Washington, DC: American Geophysical Union. https://doi.org/10.1029/GM125p0353

Bracewell, R. N. (2000). *The Fourier transform and its applications* (pp. 1–616). New York: McGraw-Hill Book Company.

Crow, E. L., & Shimizu, K. (1988). *Lognormal distributions: Theory and applications* (pp. 1–387). New York: Marcel Dekker.

Eastwood, J. P., Biffis, E., Hapgood, M. A., Green, L., Bisi, M. M., & Bentley, R. D. (2017). The economic impact of space weather: Where do we stand? *Risk Analysis*, *37*(2), 206–218. https://doi.org/10.1111/risa.12765

Efron, B., & Tibshirani, R. J. (1993). *An introduction to the bootstrap*. Dordrecht, Netherlands: Springer Science+Business Media.

Egbert, G. D. (2007). Robust electromagnetic transfer functions estimates. In D. Gubbins & E. Herrero-Bervera (Eds.), *Encyclopedia of geomagnetism and paleomagnetism* (pp. 866–870). Dordrecht, Netherlands: Springer.

Evans, R. L. (2012). Earth's electromagnetic environment: 3A. Conductivity of Earth materials. In A. D. Chave & A. G. Jones (Eds.), *The magnetotelluric method* (pp. 50–95). Cambridge, UK: Cambridge University Press.

Federal Energy Regulatory Commission (2013). Reliability standards for geomagnetic disturbances, Federal Register. *Rules and Regulations*, *78*(100), 30,747–30,762.

Ferguson, I. J. (2012). Instrumentation and field procedures. In A. D. Chave & A. G. Jones (Eds.), *The magnetotelluric method* (pp. 421–479). Cambridge, UK: Cambridge University Press.

Ferguson, I. J., & Odwar, H. D. (1997). Review of conductivity soundings in Canada, Appendix 3. In D. H. Boteler (Ed.), *Geomagnetically induced currents: Geomagnetic hazard assessment, phase II, 357 T 848A* (Vol. 3, pp. 1–121). Geological Association of Canada and Canadian Electricity Association.

Fernberg, P. (2012). *One-dimensional Earth resistivity models for selected areas of continental United States and Alaska* (pp. 1–190). Palo Alto, CA: EPRI Technical Update 1026430.

Fujii, I., Ookawa, T., Nagamachi, S., & Owada, T. (2015). The characteristics of geoelectric fields at Kakioka, Kanoya, and Memambetsu inferred from voltage measurements during 2000 to 2011. *Earth Planets Space*, *67*, 62. https://doi.org/10.1186/s40623-015-0241-z

Gates, A. E., & Glover III, L. (1989). Alleghanian tectono-thermal evolution of the dextral transcurrent Hylas zone, Virginia Piedmont, U.S.A. *Journal of Structural Geology*, *11*(4), 407–419. https://doi.org/10.1016/0191-8141(89)90018-7

Hatcher, R. D. (2005). North America: Southern and Central Appalachians. In R. C. Selley, L. Cocks, M. Robin, & I. R. Plimer (Eds.), *Encyclopedia of Geology* (pp. 72–81). Oxford, UK: Elsevier.

Hermance, J. F. (2011). Magnetotelluric interpretation. In H. K. Gupta (Ed.), *Encyclopedia of Solid Earth Geophysics* (pp. 822–829). Dordrecht, Netherlands: Springer-Verlag.

James, F. (2006). *Statistical methods in experimental physics* (pp. 1–345). Amsterdam, Netherlands: World Scientific Publishing.

Kamide, Y., & Baumjohann, W. (1993). *Magnetosphere-ionosphere coupling, physics and chemistry in space* (Vol. 23, pp. 1–178). Berlin, Germany: Springer-Verlag.

Kappenman, J. G. (2012). A perfect storm of planetary proportions. *IEEE Spectrum*, *49*, 26–31.

Kelbert, A., Egbert, G. D., & Schultz, A. (2011). IRIS DMC data services products: EMTF the magnetotelluric transfer functions, https://doi.org/10.17611/DP/EMTF

King, P. B., Beikman, H. M., & Edmonston, G. J. (1974). *Geologic map of the United States (exclusive of Alaska and Hawaii)*. United States: U. S. Geological Survey Report.

Lilley, T. (2007). Coast effect of induced currents. In D. Gubbins & E. Herrero-Bervera (Eds.), *Encyclopedia of geomagnetism and paleomagnetism* (pp. 61–65). Dordrecht, Netherlands: Springer.

Lloyd's of London (2013). *Emerging risk report: Solar storm risk to the North American electric grid* (pp. 1–22). London, UK.

Love, J. J., & Bedrosian, P. A. (2018). Extreme-event geoelectric hazard maps. In N. Buzulukova (Ed.), *Extreme Space Weather* (Chap. 9, pp. 209–230). Amsterdam, Netherlands: Elsevier.

Love, J. J., & Finn, C. A. (2011). The USGS geomagnetism program and its role in space weather monitoring. *Space Weather*, *9*, S07001. https://doi.org/10.1029/2011SW000684

Love, J. J., Rigler, E. J., Pulkkinen, A., & Riley, P. (2015). On the lognormality of historical magnetic storm intensity statistics: Implications for extreme-event probabilities. *Geophysical Research Letters*, *42*, 6544–6553. https://doi.org/10.1002/2015GL064842

Love, J. J., Pulkkinen, A., Bedrosian, P. A., Jonas, S., Kelbert, A., Joshua Rigler, E., … Kozyra, J. U. (2016). Geoelectric hazard maps for the continental United States. *Geophysical Research Letters*, *43*, 9415–9424. https://doi.org/10.1002/2016GL070469

McKay, A. J., & Whaler, K. A. (2006). The electric field in northern England and southern Scotland: Implications for geomagnetically induced currents. *Geophysical Journal International*, *167*(2), 613–625. https://doi.org/10.1111/j.1365-246X.2006.03128.x

Menvielle, M., Iyemori, T., Marchaudon, A., & Nosé, M. (2011). Geomagnetic indices. In M. Mandea & M. Korte (Eds.), *Geomagnetic observations and models* (pp. 183–227). New York: Springer.

Mitzenmacher, M. (2004). A brief history of generative models for power law and lognormal distributions. *Internet Mathematics*, *1*(2), 226–251. https://doi.org/10.1080/15427951.2004.10129088

Molinski, T. S. (2002). Why utilities respect geomagnetically induced currents. *Journal of Atmospheric and Solar-Terrestrial Physics*, *64*(16), 1765–1778. https://doi.org/10.1016/S1364-6826(02)00126-8

Murphy, B. S., & Egbert, G. D. (2017). Electrical conductivity structure of Southeastern North America: Implications for lithospheric architecture and Appalachian topographic rejuvenation. *Earth and Planetary Science Letters*, *462*, 66–75. https://doi.org/10.1016/j.epsl.2017.01.009

National Science and Technology Council (2015). *National space weather action plan* (pp. 1–38). Washington, DC: Executive Office.

Newman, M. E. J. (2005). Power laws, Pareto distributions and Zipf's law. *Contemporary Physics*, *46*(5), 323–351. https://doi.org/10.1080/00107510500052444

North American Electric Reliability Corporation (1990). March 13, 1989 geomagnetic disturbance. In *1989 System Disturbances* (pp. 36–60). Princeton, NJ.

North American Electric Reliability Corporation (2014). *Benchmark geomagnetic disturbance event description* (pp. 1–26). Atlanta, GA.

Ogawa, Y., Jones, A. G., Unsworth, M. J., Booker, J. R., Lu, X., Craven, J., … Farquharson, C. (1996). Deep electrical conductivity structures of the Appalachian Orogen in the southeastern U.S. *Geophysical Research Letters*, *23*(13), 1597–1600. https://doi.org/10.1029/95GL03601

Palacky, G. J. (1988). Resistivity characteristics of geologic targets. In M. N. Nabighian (Ed.), *Electromagnetic methods in applied geophysics: Theory* (Vol. 1, chap. 3, 53–129). Tulsa, OK: Society of Exploration Geophysicists.

Panel on Seismic Hazard Analysis (1988). *Probabilistic seismic hazard analysis* (pp. 1–97). Washington, DC: National Academy Press.

Piccinelli, R., & Krausmann, E. (2014). *Space weather and power grids—A vulnerability assessment1* (pp. 1–53). Luxembourg: European Union.
Pirjola, R. (2002). Review on the calculation of surface electric and magnetic fields and of geomagnetically induced currents in ground-based technological systems. *Surveys in Geophysics*, *23*(1), 71–90.
Pirjola, R. (2013). Practical model applicable to investigating the coast effect on the geoelectric field in connection with studies of geomagnetically induced currents. *Advances in Applied Physics*, *1*(1), 9–28.
Pulkkinen, A., Bernabeu, E., Eichner, J., Beggan, C., & Thomson, A. W. P. (2012). Generation of 100-year geomagnetically induced current scenarios. *Space Weather*, *10*, S04003. https://doi.org/10.1029/2011SW000750
Pulkkinen, A., Pirjola, R., & Viljanen, A. (2008). Statistics of extreme geomagnetically induced current events. *Space Weather*, *6*, S07001. https://doi.org/10.1029/2008SW000388
Rast, N. (1989). The evolution of the Appalachian chain. In A. W. Bally & A. R. Palmer (Eds.), *The geology of North America: An overview* (Vol. A, pp. 323–348). Boulder, CO: Geological Society of America. https://doi.org/10.1130/DNAG-GNA-A.323
Samuelsson, O. (2013). *Geomagnetic disturbances and their impact on power systems* (pp. 1–18). Lund, Sweden: Ind. Elec. Eng. Auto., Lund University.
Schultz, A. (2010). A continental scale magnetotelluric observatory and data discovery resource. *Data Science Journal*, *8*, IGY6–IGY20.
Schultz, A., Egbert, G. D., Kelbert, A., Peery, T., Clote, V., Fry, B., … Staff of the National Geoelectromagnetic Facility and their Contractors (2006). USArray TA magnetotelluric transfer functions. https://doi.org/10.17611/DP/EMTF/USARRAY/TA
Schwalenberg, K., Rath, V., & Haak, V. (2002). Sensitivity studies applied to a two-dimensional resistivity model from the Central Andes. *Geophysical Journal International*, *150*(3), 673–686. https://doi.org/10.1046/j.1365-246X.2002.01734.x
Smolka, A. (2006). Natural disasters and the challenge of extreme events: Risk management from an insurance perspective. *Philosophical Transactions of the Royal Society of London. Series A*, *364*, 2147–2165.
Stratton, J. A. (1941). *Electromagnetic theory* (pp. 1–615). New York: McGraw-Hill Book Company.
Turcotte, D. L. (1997). *Fractals and chaos in geology and geophysics* (pp. 1–416). Cambridge, UK: Cambridge University Press.
Varnes, D. J. (1984). *Landslide hazard zonation: A review of principles and practices* (pp. 1–63). Paris, France: United Nations Educational, Scientific and Cultural Organization.
Veselovsky, I. S., Dmitriev, A. V., & Suvorova, A. V. (2010). Algebra and statistics of the solar wind. *Cosmic Research*, *48*, 113–128.
Watermann, J., Rasmussen, O., Stauning, P., & Gleisner, H. (2006). Temporal versus spatial geomagnetic variations along the west coast of Greenland. *Advances in Space Research*, *37*(6), 1163–1168. https://doi.org/10.1016/j.asr.2005.08.019
Wei, L. H., Homeier, N., & Gannon, J. L. (2013). Surface electric fields for North America during historical geomagnetic storms. *Space Weather*, *11*, 451–462. https://doi.org/10.1002/swe.20073
Weidelt, P., & Chave, A. D. (2012). The magnetotelluric response function. In A. D. Chave & A. G. Jones (Eds.), *The magnetotelluric method* (pp. 122–164). Cambridge, UK: Cambridge University Press.
Whitmeyer, S. J., Fichter, L. S., & Pyle, E. J. (2007). New directions in Wilson Cycle concepts: Supercontinent and tectonic rock cycles. *Geosphere*, *3*(6), 511–526. https://doi.org/10.1130/GES00091.1
Williams, M. L., Fischer, K. M., Freymueller, J. T., Tikoff, B., Tréhu, A. M., et al. (2010). *Unlocking the secrets of the North American continent: An EarthScope science plan for 2010–2020* (pp. 1–78). EarthScope.
Yoshino, T. (2011). Electrical properties of rocks. In H. K. Gupta (Ed.), *Encyclopedia of solid earth geophysics* (pp. 270–276). Dordrecht, Netherlands: Springer-Verlag.